Phase change dynamics in a cylinder containing hybrid nanofluid and phase change material subjected to a rotating inner disk

Fatih Selimefendigil[a,*], Hakan F. Öztop[b], Mohammad Hossein Doranehgard[c], Nader Karimi[d,e]

[a] *Department of Mechanical Engineering, Celal Bayar University, 45140 Manisa, Turkey*
[b] *Department of Mechanical Engineering, Technology Faculty, Fırat University, 23119 Elazığ, Turkey*
[c] *Department of Civil and Environmental Engineering, School of Mining and Petroleum Engineering, University of Alberta, Edmonton, Alberta, T6G 1H9, Canada*
[d] *School of Engineering and Materials Science, Queen Mary University of London, Mile End, E1 4NS, United Kingdom*
[e] *James Watt School of Engineering, University of Glasgow, Glasgow G12 8QQ, United Kingdom*

Abstract

In this numerical study, the phase change dynamics of a 3D cylinder containing hybrid nanofluid and phase change material (PCM) is investigated with a finite element solver. The PCM consists of spherical encapsulated paraffin wax, and the flow is under the forced convection regime. The dynamic features of the phase change process are studied for different values of the Reynolds number (between Re=100 and 300), the rotational Reynolds number of the inner disk (Rew=0 and 300), and the size of the rotating disk (length between 0.1L and 0.55L; height between 0.001H2 and 0.4H2). The flow dynamics and separated flow regions are found to be greatly influenced by the rotational speed and size of the inner disk. As Re is increased, the difference between the transition times at different rotational disk speeds decreases. At Re=100, a 21% reduction in the phase transition time is observed

* Corresponding author, Tel:+90 2362012370
Email addresses: fatih.selimefendigil@cbu.edu.tr (Fatih Selimefendigil), hfoztop1@gmail.com (Hakan F. Öztop), doranehg@ualberta.ca (Mohammad Hossein Doranehgard), n.karimi@qmul.ac.uk (Nader Karimi)

when the inner disk rotates at the highest speed as compared to the motionless case. Up to a 26% variation in the phase transition time occurs when the size of the inner rotating disk is varied. A 5 input-1 output feed-forward artificial neural network is applied to achieve fast and reliable predictions of the phase change dynamics. This study shows that introducing rotational effects can have a profound effect on the phase change dynamics of a hybrid nanofluid system containing phase change material.

Keywords: rotational surface, phase change, CFD, finite element method, artificial neural network, hybrid particles

---

Nomenclature

k thermal conductivity

H cylinder height

L cylinder length

L_f latent heat of fusion

n unit normal vector

Nu Nusselt number

p pressure

$L_{1,2}$ disk radius

Pr Prandtl number

Re Reynolds number

Rew rotational Reynolds number

t time

T temperature

T_m melting temperature

$u,\ v,\ w$ velocity components

$r,\ z$ cylindrical coordinates

Greek Characters

ν kinematic viscosity

ρ density of the fluid

ϕ solid volume fraction

ω rotational speed

Subscripts

c cold

h hot

m average

nf nanofluid

p solid particle

1. Introduction

Energy applications involving phase change material (PCM) equipped products have been gaining attention recently due to their performance enhancement potential. Thermal energy (TE) storage and management are two major areas that are applicable to various energy systems such as in solar power, refrigeration, electronic cooling, waste heat recovery, building energy, agriculture and many others. Due to the low cost and favorable heat transfer (HT) characteristics, packed bed latent heat storage (HS) is considered a promising technology. Many methods can improve the performance features of PCM embedded TE systems. In the review of Khan et al. [1], different methods for influencing the thermo-physical properties of PCMs were presented such as using fins, high conductivity additives and various arrangement of PCMs in TE systems. Thermal utilization of PCM was explored by considering different techniques and accounting for stability issues. Sharma et al. [2] reviewed PCM installed TE systems in diverse applications such as in waste heat, building and solar air heaters. Enhancing the thermal performance of PCMs by using internal fins, metallic foams and nano particles was considered in the review by Sahoo et al. [3]. Heat sinks with PCM enhancement techniques were considered for constant and variable loads while metallic foams offered several advantageous. Fins with PCM have been considered in heat sinks [4, 5], photovoltaic panels [6, 7] and building applications [8, 9].

Recently, nano-sized particles have been used in HT fluids for TE systems to improve performance. Many nanofluid types have been evaluated and experimental correlations for the effective thermophysical properties have been derived [10]. Many advanced simulation methods have been developed and tested for accurate modeling of TE systems using nanofluids [11–15]. The utilization of nanotechnology in PCM embedded systems has been considered in various TE systems [16]. In the review of Rostami et al. [17], PCM characteristics including nano-PCMs on TE storage and natural convection were critically discussed. Through numerical simulations, Khodadadi and Hosseinizadeh [18] showed performance improvement for freezing of water by using CuO nanoparticles in a cavity with numerical simulations. Other studies that have considered the use of nanoparticles with PCM can be found in Refs. [19–27].

The performance of PCM embedded systems can be enhanced by changing the geometrical features along with the thermophysical properties of the HT fluid. In TE systems with embedded latent heat storage units with encapsulated PCM, dynamic walls can be implemented to improve the performance. Rotating surfaces have been considered in many TE systems especially for convective HT applications. Although the thermal system performance can be improved via passive methods such as changing the geometry of the TE systems and installing static elements such as internal fins, metal foams, the use of dynamic walls or objects opens up new opportunities for further improvements. A rotating type object has been shown to affect the convective HT thermal performance via adjustments in the rotational speed, size and location of the object [28, 29]. Certain locations and rotational direction of the cylinder have been found to assist the convection in TE systems. The combined effects of using nanofluids and surface rotations have been considered in many studies for HT improvement in TE systems [30, 31].

The present work considers the effects of using a rotating inner disk on the performance of a PCM embedded thermo-fluid system. The effects of rotation of the inner disk and of its geometrical parameters on the dynamic features of the phase change process are numerically assessed. The effects of fluid velocity and its interaction with the rotation of the inner disk surface on the flow features are analyzed. The numerical simulations are validated against an experimental study of the phase change process. With the diverse use of PCMs in TE systems such as in electronic cooling, solar energy applications, heat exchangers, the thermal management of the phase change process via a rotating inner disk and nanofluid is novel and may be used to enhance the performance of PCM embedded energy systems.

2. Computational study

2.1. System configuration

The characteristics of a PCM-equipped cylinder under the effects of a rotating inner disk is analyzed. The height and radius of the PCM included region is hpcm and L. The rotating disk has inner and outer radius of L1d and L2d while heights are H1d and H2d. The rotational speed (Rs) of the inner disk is ω. Here, H1 and H2 denote the distance of the PCM region from the outlet and inlet, respectively. A hybrid nanofluid (with Ag and MgO nanoparticles at solid volume fraction of 2%) enters the cylinder with a velocity of ug and a temperature of Tg. Experimental correlations for the effective nanofluid properties were used as given in [32]. Spherical shaped encapsulated paraffin wax is considered as the PCM with a radius of 30 mm. Table 1 lists the thermophysical properties.

2.2. Governing equations and boundary conditions

A single phase model of nanofluid is used with Newtonian and incompressible fluid assumptions. Effects such as free convection, thermal radiation and viscous dissipation are ignored.

A hybrid nanofluid containing binary particles of Ag and MgO was used. The potential of using hybrid nanofluids has been shown in various studies of thermal engineering. They are preferred for their synergistic effects, cost and advantages of one or more types of nanoparticles in the base fluid [33–36]. In studies with nanofluid, an accurate description of the thermophysical properties is important. The experimental data fit from Ref.[32] was used to derive correlations for the thermal conductivity (k_{nf}) and viscosity (μ_{nf}) of the hybrid nanofluid. They are defined as [32]:

$$k_{nf} = \left(\frac{0.1747 \times 10^5 + \phi}{0.1747 \times 10^5 - 0.1498 \times 10^6 \phi + 0.1117 \times 10^7 \phi^2 + 0.1997 \times 10^8 \phi^3} \right) k_f, \tag{1}$$

$$\mu_{nf} = \left(1 + 32.795\phi - 7214\phi^2 + 714600\phi^3 - 0.1941 \times 10^8 \phi^4\right) \mu_f. \tag{2}$$

where ϕ is the the total concentration of nanoparticles and is taken as 2%.

In the fluid domain, the conservation equations are [37]:

$$\nabla.\mathbf{u} = \mathbf{0} \tag{3}$$

$$\begin{aligned} \rho\left(\mathbf{u}.\nabla\right)\mathbf{u} &= \nabla.\left[-p\mathbf{I} + \mathbf{K}\right] + F \\ \mathbf{K} &= \mu\left(\nabla\mathbf{u} + \left(\nabla\mathbf{u}\right)^T\right) \end{aligned} \tag{4}$$

$$\rho C_p \frac{\partial T}{\partial t} + \rho C_p \mathbf{u}.\nabla T = \nabla.\left(k\nabla T\right) \tag{5}$$

For the PCM region:

$$\nabla.\mathbf{u} = \mathbf{0} \tag{6}$$

$$\begin{aligned}
&\frac{1}{\varepsilon_p}\rho\left(\mathbf{u}.\nabla\right)\mathbf{u}\frac{1}{\varepsilon_p} = \nabla.\left[-p\mathbf{I}+\mathbf{K}\right] - \left(\mu\kappa^{-1}+\beta_p\rho|\mathbf{u}|\right)\mathbf{u}+F \\
&\mathbf{K} = \mu\frac{1}{\varepsilon_p}\left(\nabla\mathbf{u}+\left(\nabla\mathbf{u}\right)^T\right)
\end{aligned} \tag{7}$$

and with the Kozeny-Carman permeability given as:

$$\kappa = \frac{d_p^2}{180}\frac{\varepsilon_p^3}{(1-\varepsilon_p)^2} \tag{8}$$

A phase change function α is defined with a value of 0 for $T < (T_m - \Delta T_m/2)$ and 1 for $T > (T_m + \Delta T_m/2)$. The energy equation is given as:

$$\rho C_p\frac{\partial T}{\partial t} + \rho C_p\mathbf{u}.\nabla T = \nabla.\left(k\nabla T\right). \tag{9}$$

with the thermo-physical properties as:

$$\begin{aligned}
&\theta = 1-\alpha, \quad \rho = \theta\rho_{f1} + (1-\theta)\rho_{f2}, \\
&C_p = \frac{1}{\rho}\left(\theta\rho_{f1}C_{p,f1} + (1-\theta)\rho_{f2}C_{p,f2}\right) + L\frac{\partial\alpha_m}{\partial T}, \\
&k = \theta k_{f1} + (1-\theta)k_{f2}, \quad \alpha_m = \frac{1}{2}\frac{(1-\theta)\rho_{f2} - \theta\rho_{f1}}{\theta\rho_{f1} + (1-\theta)\rho_{f2}}.
\end{aligned} \tag{10}$$

In the above derivation, $f1$, $f2$ and L are the phases and latent heat of fusion. In between the phases, non-equilibrium HT in porous media interface is considered. Here, two equations for the phases and additional source terms are given [38, 39]:

$$\theta_p\rho_s C_{p,s}\frac{T_s}{\partial t} + \nabla.\mathbf{q_s} = q_{sf}\left(T_f - T_s\right) + \theta_p Q_s, \tag{11}$$

$$\mathbf{q_s} = -\theta_p k_s\nabla T_s, \tag{12}$$

$$\begin{aligned}
&(1-\theta_p)\rho_f C_{p,f}\frac{T_f}{\partial t} + (1-\theta_p)\rho_f C_{p,f}\mathbf{u_f}.\nabla T_f + \\
&+\nabla.\mathbf{q_f} = q_{sf}(T_s - T_f) + (1-\theta_p)Q_f,
\end{aligned} \tag{13}$$

$$\mathbf{q_f} = -(1-\theta_p)k_f\nabla T_f. \tag{14}$$

In the above equations, $\mathbf{q_f}, \mathbf{q_s}, \theta_p$ denote the conductive heat fluxes of the solid and fluid and porous media SVF. The interstitial convective HT coefficient is given by the term q_{sf} while Q_s and Q_f are the solid and fluid heat sources, respectively. For a spherical pellet bed [38, 39]:

$$q_{sf} = a_{sf}h_{sf} \tag{15}$$

The interstitial HT coefficient is given by [38, 39]:

$$\frac{1}{h_{sf}} = \frac{2r_p}{k_f\mathrm{Nu}} + \frac{2r_p}{\beta k_s}. \tag{16}$$

The value of β is taken to be 10 for spherical particles. The fluid-to-solid Nu number is: [40]:

$$\mathrm{Nu} = 2 + 1.1\mathrm{Pr}^{1/3}\mathrm{Re}_p^{0.6}. \tag{17}$$

The Prandtl number and Reynolds number of the particles are:

$$\mathrm{Pr} = \frac{\mu C_{p,f}}{k_f}, \quad \mathrm{Re}_p = \frac{2r_p\rho_f|u_f|}{\mu}. \tag{18}$$

The relevant non-dimensional parameters are the Reynolds number (Re) for the fluid and the rotational Reynolds number (Rew) for the rotating inner disk, both of which are varied in our simulations. They are given as:

$$\mathrm{Re} = \frac{u_g L\rho}{\mu}, \quad \mathrm{Rew} = \frac{\omega(L1d)^2\rho}{\mu} \tag{19}$$

The Re number and rotational Re of the inner disk are the varied during the simulation. The fluid velocity at the inlet is ug and the temperature is Tg=336 K. The model is axis-symmetrical with $\frac{\partial T}{\partial r} = 0$. The walls of the cylinder are adiabatic with no-slip boundary conditions (BCs) as, $u = w = 0$, $\frac{\partial T}{\partial n} = 0$. A pressure outlet is used at the exit. The inner disk is rotating with Rs of ω. The velocity of the tangentially moving wall is 0 while the angular component of the moving wall is ωr. The rotating disk is also considered adiabatic such that $\frac{\partial T}{\partial n} = 0$ with an initial temperature of 303 K.

2.3. Solution method and code validations

To solve the above GEs, the GWR-finite element method is used. The field variable (Ψ) appropriations are performed as:

$$\psi = \sum_{n=1}^{N^s} \Phi_n^s \Psi_n \tag{20}$$

where Φ^s is the shape function and Ψ is the element nodal value. Different ordered Lagrange FEM is considered. The time dependent part is treated by utilizing a second order backward differentiation scheme. A time step size of 0.1 min is used. Time step independence of the solution is also assured. A commercial computational fluid dynamics code Comsol was used with built-in modules for multi-physics simulations [39]. Tests for grid independence were conducted and the results are given in Figure 2 (a) for two different values of Rs of the inner disk. Grid system G4 with 63412 elements is selected. At the interface regions and near the walls, the mesh is finer as shown in Figure 2 (b). Validation is conducted by using results for the phase change process and impacts of rotation on the convective HT. First, results available in Ref. [41] are used. In the study, experimental analysis for PC process in a differentially heated cavity was performed. The role of free convection for PC of pure metal was explored while the two vertical walls of the rectangular test section were maintained at different temperatures. The amount of solidified volume is a time dependent quantity and it depends on the solidified volume (V), Rayleigh number (Ra), total volume (V_0), aspect ratio (AT) and dimensionless time (τ) as:

$$\frac{V}{V_0} = 2.91\tau^{0.53}\mathrm{Ra}^{-0.05}A^{-0.36} \tag{21}$$

Figure 3 compares the solidified volume at different dimensionless times Compared with experimental data, the greatest difference observed as -9.3% at $\tau^{0.53}\mathrm{Ra}^{-0.05}A^{-0.36} = 0.114$. In another study, Roslan et al. [42] explored the effects of rotation on convective HT by using an inner cylinder in square cavity. They considered a differentially heated enclosure while rotational speed and size effects of the inner cylinder on the convective HT features were explored using FEM. Comparison of the average Nu is given in Figure 5 for two different configurations (cylinder size and Rs). In both cases, the difference is limited to under 3%. The results reinforce the capability of the code in simulating the PC process and the rotational effects of the inner surfaces on convection.

2.4. Performance estimation with artificial neural network

Artificial neural network (ANN) modeling is widely used in energy systems and thermal engineering for flow control, performance prediction and system identification. Many different soft computing methods and ANN techniques have been demonstrated for accurate performance predictions of energy systems [43–49]. Many steps involved in soft computing methods are similar such as specification of the input-output data set, activation functions, learning algorithms and validation tests. The Levenberg-Marquardt

(LM) techniques with backpropogation (BP) is chosen here as learning algorithm [50]. A mathematical model for the input-output relation of the data set can be derived with an ANN. The network structure consists of multiple different layers (input, hidden and output layers) and different numbers of neurons are used in the hidden layers. They can be adjusted along with the network parameters during the training phase. The network performance at each iteration step is checked by comparing the network output and data from simulations or experiments while the weights of the ANN are updated. A learning algorithm with backpropagation is used for adjusting the weights of ANN. Each neuron output is given as [47]:

$$Y = G\left(\sum_{i=1}^{M} X_i W_i + S\right) \tag{22}$$

where Y, G and M represent the output data, activation function and data number while X, W and S are the input, weight and bias term, respectively. Different criteria may be applied to test the performance of different ANN models. The mean square error (MSE) and coefficient of determination (R^2) are commonly used [51]:

$$\mathrm{MSE} = \frac{1}{M}\sum_{i=1}^{M}\left(y_i^{CFD} - y_i^{N}\right)^2, \tag{23}$$

$$\mathrm{R}^2 = 1 - \frac{\sum_{i=1}^{M}\left(y_i^{CFD} - y^{N}\right)^2}{\sum_{i=1}^{M}\left(y_i^{CFD} - \bar{y}^{N}\right)^2}. \tag{24}$$

3. Results and discussion

The effects of using a rotating object in a PCM filled cylinder on the performance enhancement are numerically assessed. The Rs of the disk is ω

and is varied during the simulation. The dynamic characteristics of the phase change process are studied for various values of Re (between 100 and 300), Rew of the disk (0 and 300), and size of the rotating disk (length between 0.1L and 0.55L; height between 0.001H2 and 0.4H2). The time evolution of the liquid fraction (Lf) and phase completion time are analyzed. ANN-based estimation is performed to determine the time dependent characteristics of the liquid fraction for various values of input parameters such as Rew and the size of the inner rotating disk.

3.1. ***CFD simulation results***

Figure 5 shows the impacts of Re on the flow patterns variation at two different values of Rew. When the inner disk is not rotating, the flow separates at the edge of the disk away from the inlet and its extent increases with Re. However, in the presence of rotational effects due to the inner disk surfaces, the separated flow region extending through the PCM domain becomes significant. As Re is increased, the size of the vortex at the interface becomes reduced and the recirculation zone is suppressed. The recirculation zone becomes larger at the edges of the rotating disk as Rs increases (Figure 6). The separated flow region moves toward the vertical wall of the cylindrical container for higher Rew. Time evolutions of the PCM temperatures for different Rew are presented in Figure 7. Due to the recirculation zones caused by rotation of the inner disk, the PCM temperatures are significantly affected in the inner part and toward the walls when the disk is rotating at the highest speed. Variation of the PCM temperatures at two points (in the axis- symmetric location and in the vertical wall) are shown in Figure 8 for various values of Re and Rs of the inner disk. In the absence and presence of rotational effects, when the fluid velocity increases, the phase change process speeds up. However, the effects of Rw on the phase change differs at the mid point (axis-symmetrical location) and in the wall location. At the wall location, phase transition becomes rapid with increasing Rew while the effects is reversed at mid point location. Time evolution of the liquid fraction at two different values of Rew is given in Figure 9. At t=40 min full phase transition is achieved when rotational effects of the inner disk are considered at the highest speed. Near the wall region and interior of the cylinder, rotational effects on the phase transition become dominant. The dynamic characteristics of the liquid fraction (Fr) for various Re at two different values of Rew of 0 and 300 are shown in Figure 10. The values of Fr approach for higher Re for both values of Rew. A saturation type curve is obtained while the discrepancy between different Re on Fr becomes different when rotational effects are considered. Full phase transition time (tr) with different Re and Rew are given in Figure 11. The effects of Rew on tr becomes dominant for lower fluid velocities but at Re=300, its impacts are negligible. There is a 21% reduction in the full transition time at Re=100 when rotational effects at the highest speed are considered as compared to a motionless disk. When the effects of Rew are considered, the full phase transition time first increases up to Rew=50 but decreases thereafter. This is attributed to the balance between vortex formation which has negative effects on the phase change process while for higher rotational speeds, the fluid velocity near the rotation surfaces becomes higher, causing a positive impact on the phase change process. There is almost a 16 % reduction in tr when the configuration with higher Rs is compared with the case of a motionless disk.

Geometrical parameters of the rotating disk have also affected the phase change process. The flow pattern variations with varying length and height of the rotating disk are given in Figure 12. The separated flow region becomes significant and occupies a large portion of the PCM region for L2d=0.3L while it is smallest for L2d=0.1L. At L=0.55L, the region approaches the vertical wall of the cylinder. When the height is increased, an elongation of the vortex region in the flow direction is observed. At the highest height, its size is reduced in the radial direction. Varying the length and height of the rotating inner disk has opposite effects when the time evolution of the temperatures at the wall region is compared to the location at the mid-axis plane. At the wall location, the phase change process becomes faster for higher values of length and height of the inner rotating disk. The dynamic features of liquid fraction are highly affected with varying length as compared to height (Figure 14). The Fr values become lower with higher length of the rotating disk most of the time. Full phase transition shows non-monotonic behavior with varying geometrical parameters of the inner disk. When the length is increased up to L2d=0.3L, the value of tr is reduced, indicating that the phase change process is relatively fast. Even though the recirculation region becomes larger, due to the increased fluid velocity with rotation, it is lower. However, for disk lengths greater than L2d=0.3L, the value of tr increases, a trend attributed to the movement of the vortex region toward the vertical walls, resulting in an inefficient phase change process. There is a 26% reduction in the value of tr when cases with L2=0.1H and L2=0.3H are compared. When the height is increased to H2d=0.1L, the value of tr reduces owing to a reduction of the vortex size in the radial direction.

However, further increases of the rotating disk height resulted in longer full phase transition times. The variation in the tr values becomes 21% while the lowest tr value is achieved at H2d=0.1H2.

3.2. ***ANN prediction***

Feed-forward ANNs are used for performance predictions and dynamic feature extraction of the PCM-equipped energy system with a rotating disk. As input, five input data is selected. They are Re, Rew, height /length of the rotating disk and time (t in minutes). As network output, the liquid fraction (Lr) is selected. Here, 1877 CFD simulation datasets are generated with 70% used for training and the remainder used for testing and validation. As the activation function, a hyperbolic tangent sigmoid function ($f(x) = 1/(1 + e^{(-x)})$) is used while LM-BP is selected as the learning algorithm. The number of neurons in the hidden layer is determined according to their performances in the hidden layer; it is chosen to be 15 (Table 2) for training. Figure 16 shows a schematic view of the ANN structure with different layers and network features. ANN performance with 15 neurons and for various data sets (training, validation and testing) is given in Table 3. Lower values of MSE are obtained while R^2 approach 1. Comparison of network performance estimation for various Rew of the inner disk is given in Figure 18 (a). Effects of varying the length of the rotating disk on the full phase transition time is given in Figure 18 (b) by using CFD simulation and ANN estimation model. These results show that the ANN model has higher prediction accuracy when analyzing the effects of using inner rotating cylinder on the phase change dynamics. Variations of the full phase completion time and and time dependent variation of the liquid fraction can be estimated by using the ANN model where time is used as an additional parameter.

4. Conclusions

In the present study, the effect of using a rotating inner disk on the performance of a PCM-equipped thermo-fluid system containing a hybrid nanofluid. The following conclusions can be drawn as:

- Introducing rotational surface effects of the inner disk significantly affected the flow features. There is a 21% reduction in the phase transition time at Re=100 when the inner disk is rotating at the highest speed as compared to the motionless cases.

- Vortex formation occurs within the system at higher rotational speeds due to the resultant changes in the phase change process. At higher Rew, the phase change process is accelerated with up to a 16 % reduction in the transition time

- Separated flow zones occupying the PCM region are affected by the size of the rotating inner disk.

- The dynamic properties of the liquid fraction are influenced more by varying the length than by varying the height of the inner disk. When configurations at disk sizes of L2=0.1H and L2=0.3H are compared, there is a 26% reduction in the phase transition time but this drops to 21% when varying the height of the rotating disk.

- Feed-forward ANN modeling with 15 neurons in the hidden layer is shown to provide fast and accurate estimation results.

In future work, this study can be extended to include different thermal boundary conditions, different PCMs, geometric modifications in the main reactor and the PCM region, effects of HT fluid inlet temperature variations and using various types of hybrid nanofluids. This should increase the applicability of the present results.

References

[1] Z. Khan, Z. Khan, A. Ghafoor, A review of performance enhancement of PCM based latent heat storage system within the context of materials, thermal stability and compatibility, Energy conversion and management 115 (2016) 132–158.

[2] A. Sharma, V. V. Tyagi, C. Chen, D. Buddhi, Review on thermal energy storage with phase change materials and applications, Renewable and Sustainable energy reviews 13 (2009) 318–345.

[3] S. K. Sahoo, M. K. Das, P. Rath, Application of TCE-PCM based heat sinks for cooling of electronic components: A review, Renewable and Sustainable Energy Reviews 59 (2016) 550–582.

[4] S. Hosseinizadeh, F. Tan, S. Moosania, Experimental and numerical studies on performance of pcm-based heat sink with different configurations of internal fins, Applied Thermal Engineering 31 (2011) 3827–3838.

[5] R. Akhilesh, A. Narasimhan, C. Balaji, Method to improve geometry for heat transfer enhancement in PCM composite heat sinks, International Journal of Heat and Mass Transfer 48 (2005) 2759–2770.

[6] S. Khanna, K. Reddy, T. K. Mallick, Optimization of finned solar photovoltaic phase change material (finned pv pcm) system, International Journal of Thermal Sciences 130 (2018) 313–322.

[7] F. Bayrak, H. F. Oztop, F. Selimefendigil, Experimental study for the application of different cooling techniques in photovoltaic (pv) panels, Energy Conversion and Management 212 (2020) 112789.

[8] F. Souayfane, F. Fardoun, P.-H. Biwole, Phase change materials (pcm) for cooling applications in buildings: A review, Energy and buildings 129 (2016) 396–431.

[9] R. Saxena, D. Rakshit, S. Kaushik, Experimental assessment of phase change material (pcm) embedded bricks for passive conditioning in buildings, Renewable Energy 149 (2020) 587–599.

[10] K. Khanafer, K. Vafai, A review on the applications of nanofluids in solar energy field, Renewable Energy 123 (2018) 398–406.

[11] H. F. Oztop, E. Abu-Nada, Numerical study of natural convection in partially heated rectangular enclosures filled with nanofluids, International Journal of Heat and Fluid Flow 29 (2008) 1326–1336.

[12] O. A. Akbari, M. R. Safaei, M. Goodarzi, N. S. Akbar, M. Zarringhalam, G. A. S. Shabani, M. Dahari, A modified two-phase mixture model of nanofluid flow and heat transfer in a 3-D curved microtube, Advanced Powder Technology 27 (2016) 2175–2185.

[13] O. Mahian, A. Kianifar, C. Kleinstreuer, A.-N. Mohd A, I. Pop, A. Z.

Sahin, S. Wongwises, A review of entropy generation in nanofluid flow, International Journal of Heat and Mass Transfer 65 (2013) 514–532.

[14] S. A. Bagherzadeh, A. DOrazio, A. Karimipour, M. Goodarzi, Q.-V. Bach, A novel sensitivity analysis model of EANN for F-MWCNTs–Fe3O4/EG nanofluid thermal conductivity: Outputs predicted analytically instead of numerically to more accuracy and less costs, Physica A: Statistical Mechanics and Its Applications 521 (2019) 406–415.

[15] M. M. Sarafraz, M. R. Safaei, Z. Tian, M. Goodarzi, E. P. Bandarra Filho, M. Arjomandi, Thermal assessment of nano-particulate graphene-water/ethylene glycol (WEG 60: 40) nano-suspension in a compact heat exchanger, Energies 12 (2019) 1929.

[16] S. S. Sebti, M. Mastiani, H. Mirzaei, A. Dadvand, S. Kashani, S. A. Hosseini, Numerical study of the melting of nano-enhanced phase change material in a square cavity, Journal of Zhejiang University SCIENCE A 14 (2013) 307–316.

[17] S. Rostami, M. Afrand, A. Shahsavar, M. Sheikholeslami, R. Kalbasi, S. Aghakhani, M. S. Shadloo, H. F. Oztop, A review of melting and freezing processes of PCM/Nano-PCM and their application in energy storage, Energy (2020) 118698.

[18] J. Khodadadi, S. Hosseinizadeh, Nanoparticle-enhanced phase change materials (nepcm) with great potential for improved thermal energy storage, International communications in heat and mass transfer 34 (2007) 534–543.

[19] N. S. Dhaidan, J. Khodadadi, T. A. Al-Hattab, S. M. Al-Mashat, Experimental and numerical investigation of melting of nepcm inside an annular container under a constant heat flux including the effect of eccentricity, International Journal of Heat and Mass Transfer 67 (2013) 455–468.

[20] S. Mousavi, M. Siavashi, M. M. Heyhat, Numerical melting performance analysis of a cylindrical thermal energy storage unit using nano-enhanced PCM and multiple horizontal fins, Numerical Heat Transfer, Part A: Applications 75 (2019) 560–577.

[21] F. Selimefendigil, H. F. Öztop, Impacts of magnetic field and hybrid nanoparticles in the heat transfer fluid on the thermal performance of phase change material installed energy storage system and predictive modeling with artificial neural networks, Journal of Energy Storage 32 (2020) 101793.

[22] M. R. Hajizadeh, F. Selimefendigil, T. Muhammad, M. Ramzan, H. Babazadeh, Z. Li, Solidification of PCM with nano powders inside a heat exchanger, Journal of Molecular Liquids 306 (2020) 112892.

[23] F. Selimefendigil, H. F. Öztop, Mhd pulsating forced convection of nanofluid over parallel plates with blocks in a channel, International Journal of Mechanical Sciences 157 (2019) 726–740.

[24] M. Sarafraz, M. R. Safaei, A. S. Leon, I. Tlili, T. A. Alkanhal, Z. Tian, M. Goodarzi, M. Arjomandi, Experimental investigation on thermal per-

formance of a PV/T-PCM (photovoltaic/thermal) system cooling with a PCM and nanofluid, Energies 12 (2019) 2572.

[25] M. Sheikholeslami, Numerical investigation for CuO-H2O nanofluid flow in a porous channel with magnetic field using mesoscopic method, Journal of molecular liquids 249 (2018) 739–746.

[26] A. H. Al-Waeli, K. Sopian, H. A. Kazem, J. H. Yousif, M. T. Chaichan, A. Ibrahim, S. Mat, M. H. Ruslan, Comparison of prediction methods of pv/t nanofluid and nano-pcm system using a measured dataset and artificial neural network, Solar Energy 162 (2018) 378–396.

[27] M. R. Safaei, H. R. Goshayeshi, I. Chaer, Solar still efficiency enhancement by using graphene oxide/paraffin nano-PCM, Energies 12 (2019) 2002.

[28] A. I. Alsabery, T. Tayebi, A. J. Chamkha, I. Hashim, Effect of rotating solid cylinder on entropy generation and convective heat transfer in a wavy porous cavity heated from below, International Communications in Heat and Mass Transfer 95 (2018) 197–209.

[29] F. Selimefendigil, H. F. Oztop, Mixed convection of nanofluids in a three dimensional cavity with two adiabatic inner rotating cylinders, International Journal of Heat and Mass Transfer 117 (2018) 331–343.

[30] Z. Raizah, A. M. Aly, Double-diffusive convection of a rotating circular cylinder in a porous cavity suspended by nano-encapsulated phase change materials 24 (????) 100864.

[31] F. Selimefendigil, H. F. Öztop, Performance assessment of a thermoelectric module by using rotating circular cylinders and nanofluids in the channel flow for renewable energy applications, Journal of Cleaner Production 279 (2021) 123426.

[32] M. H. Esfe, A. A. A. Arani, M. Rezaie, W.-M. Yan, A. Karimipour, Experimental determination of thermal conductivity and dynamic viscosity of Ag-MgO/water hybrid nanofluid, International Communications in Heat and Mass Transfer 66 (2015) 189–195.

[33] A. A. Minea, Challenges in hybrid nanofluids behavior in turbulent flow: recent research and numerical comparison, Renewable and Sustainable Energy Reviews 71 (2017) 426–434.

[34] M. Bahiraei, M. Jamshidmofid, M. Goodarzi, Efficacy of a hybrid nanofluid in a new microchannel heat sink equipped with both secondary channels and ribs, Journal of Molecular Liquids 273 (2019) 88–98.

[35] M. Goodarzi, I. Tlili, Z. Tian, M. R. Safaei, Efficiency assessment of using graphene nanoplatelets-silver/water nanofluids in microchannel heat sinks with different cross-sections for electronics cooling, International Journal of Numerical Methods for Heat & Fluid Flow (2019).

[36] J. R. Babu, K. K. Kumar, S. S. Rao, State-of-art review on hybrid nanofluids, Renewable and Sustainable Energy Reviews 77 (2017) 551–565.

[37] F. Mohammadnejad, S. Hossainpour, A CFD modeling and investigation of a packed bed of high temperature phase change materials (PCMs)

with different layer configurations, Journal of Energy Storage 28 (2020) 101209.

[38] D. Nield, A. Bejan, Convection in Porous Media, in Convection Heat Transfer, John Wiley & Sons, Inc., Hoboken, NJ, USA, 2013.

[39] Comsol, Comsol User's Guide, 2018.

[40] N. Wakao, S. Kaguei, T. Funazkri, Effect of fluid dispersion coefficients on particle-to-fluid heat transfer coefficients in packed beds: correlation of Nusselt numbers, Chemical engineering science 34 (1979) 325–336.

[41] F. Wolff, R. Viskanta, Solidification of a pure metal at a vertical wall in the presence of liquid superheat, International journal of heat and mass transfer 31 (1988) 1735–1744.

[42] R. Roslan, H. Saleh, I. Hashim, Effect of rotating cylinder on heat transfer in a square enclosure filled with nanofluids 55 (????) 7247–7256.

[43] Y. Varol, E. Avci, A. Koca, H. F. Oztop, Prediction of flow fields and temperature distributions due to natural convection in a triangular enclosure using adaptive-network-based fuzzy inference system (anfis) and artificial neural network (ann), International Communications in Heat and Mass Transfer 34 (2007) 887–896.

[44] M. H. Ahmadi, B. Mohseni-Gharyehsafa, M. Ghazvini, M. Goodarzi, R. D. Jilte, R. Kumar, Comparing various machine learning approaches in modeling the dynamic viscosity of CuO/water nanofluid, Journal of Thermal Analysis and Calorimetry 139 (2020) 2585–2599.

[45] F. Selimefendigil, H. F. Öztop, Three dimensional unsteady heat and mass transport from six porous moist objects in a channel under laminar forced convection, Applied Thermal Engineering (2020) 116100.

[46] A. A. Ahmadi, M. Arabbeiki, H. M. Ali, M. Goodarzi, M. R. Safaei, Configuration and optimization of a minichannel using water–alumina nanofluid by non-dominated sorting genetic algorithm and response surface method, Nanomaterials 10 (2020) 901.

[47] S. A. Kalogirou, Applications of artificial neural-networks for energy systems, Applied energy 67 (2000) 17–35.

[48] S. Giwa, M. Sharifpur, M. Goodarzi, H. Alsulami, J. Meyer, Influence of base fluid, temperature, and concentration on the thermophysical properties of hybrid nanofluids of alumina–ferrofluid: experimental data, modeling through enhanced ANN, ANFIS, and curve fitting, Journal of Thermal Analysis and Calorimetry 143 (2021) 4149–4167.

[49] A. Shahsavar, S. Khanmohammadi, A. Karimipour, M. Goodarzi, A novel comprehensive experimental study concerned synthesizes and prepare liquid paraffin-Fe3O4 mixture to develop models for both thermal conductivity & viscosity: a new approach of GMDH type of neural network, International Journal of Heat and Mass Transfer 131 (2019) 432–441.

[50] C. Yu, M. T. Manry, J. Li, P. L. Narasimha, An efficient hidden layer training method for the multilayer perceptron, Neurocomputing 70 (2006) 525–535.

[51] A. H. Al-Waeli, H. A. Kazem, J. H. Yousif, M. T. Chaichan, K. Sopian, Mathematical and neural network models for predicting the electrical performance of a PV/T system, International Journal of Energy Research 43 (2019) 8100–8117.

Table 1: Thermo-physical properties of PCM

Property	Value
Melting temperature (T_m, ^oC)	60
Latent heat of fusion (L, kJ/kg)	213
Density-solid (ρ, kg/m^3)	861
Density-liquid (ρ, kg/m^3)	778
Thermal conductivity-solid (k, W/m^oC)	0.40
Thermal conductivity-fluid (k, W/m^oC)	0.15
Specific heat-solid (C_p, J/kg^oC)	1850
Specific heat-fluid (C_p, J/kg^oC)	2384

Table 2: Network performance dependence on the neuron in the hidden layer

Number of neurons	MSE -Training	R^2 -Training
10	6.806×10^{-4}	0.9973
15	1.102×10^{-4}	0.9995
25	2.767×10^{-4}	0.9986

Table 3: ANN results for training, testing and validation using 15 neurons in the hidden layer

Data Type	Number of samples	MSE	R^2
Training	1313	1.102×10^{-4}	0.9995
Validation	282	1.287×10^{-4}	0.9994
Testing	282	1.467×10^{-4}	0.9994

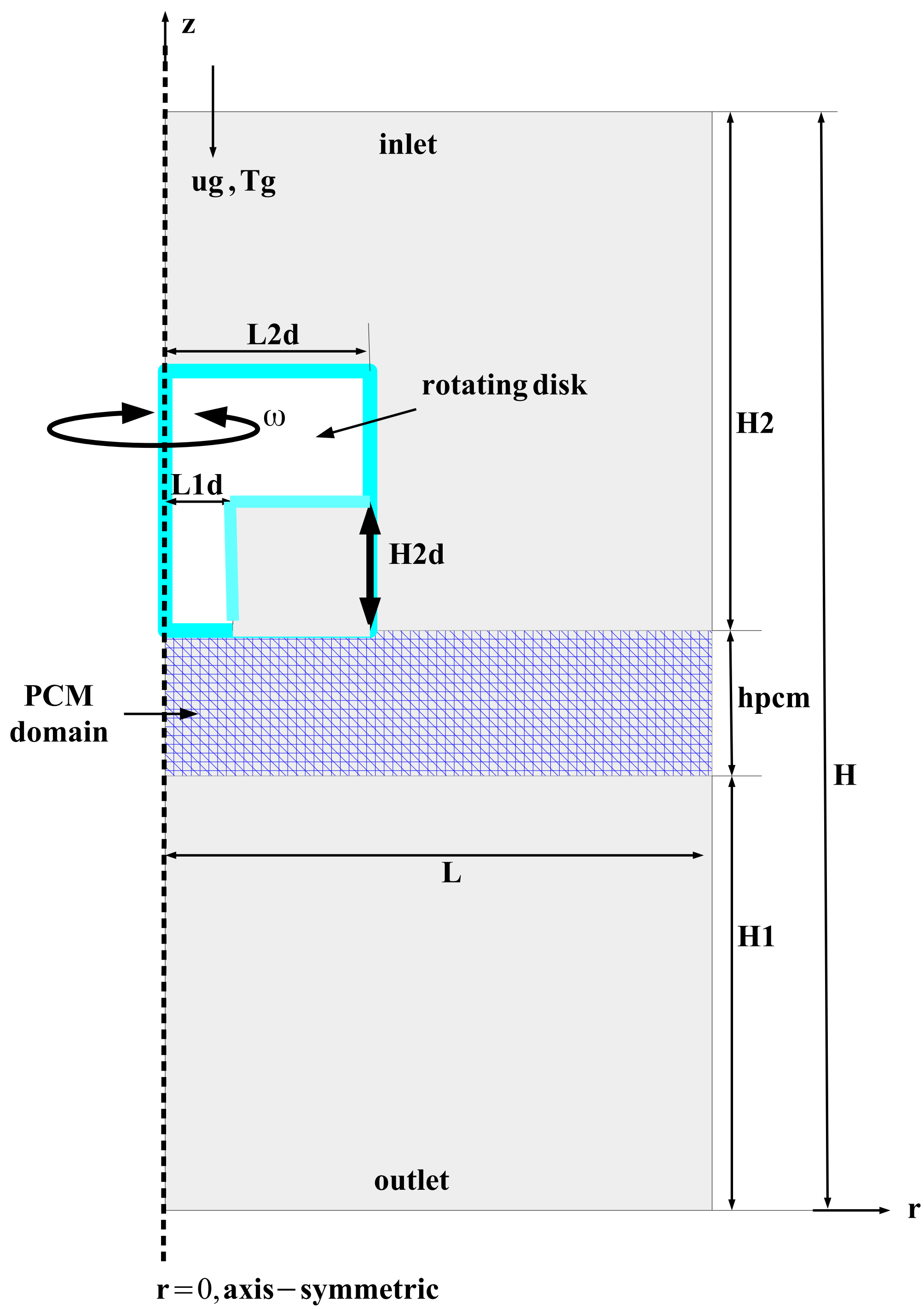

Figure 1: PCM equipped cylinder with a rotating inner disk

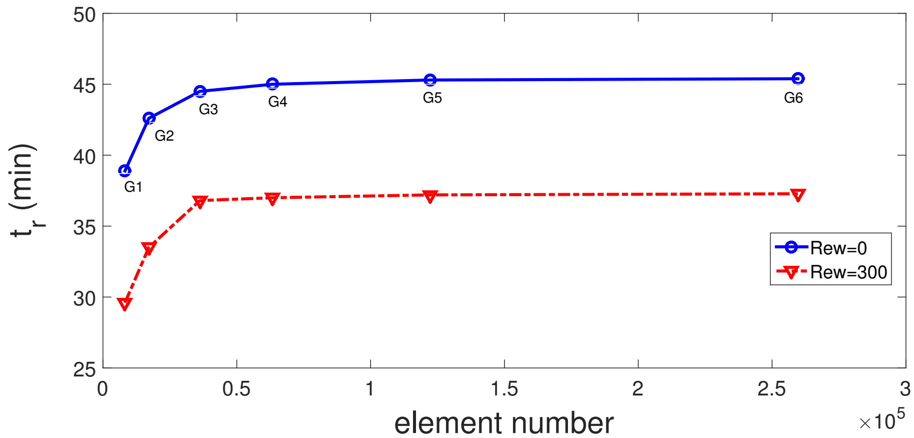

(a)

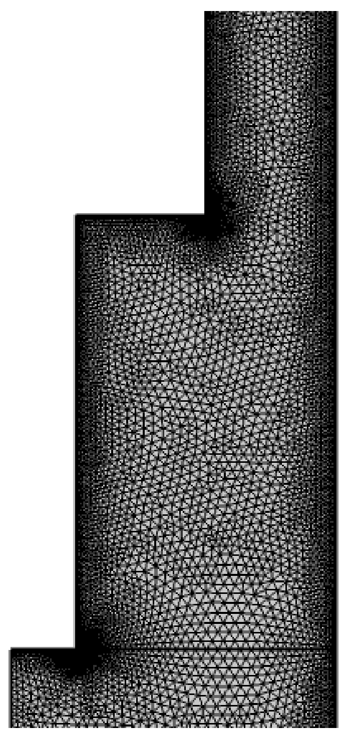

(b)

Figure 2: Numerical results for grid independence at two different values of Rew (a) ($\mathrm{Re} = 200, L1d = 0.1L, L2d = 0.5L, H2d = 0.3H2$) and distribution of grid (b)

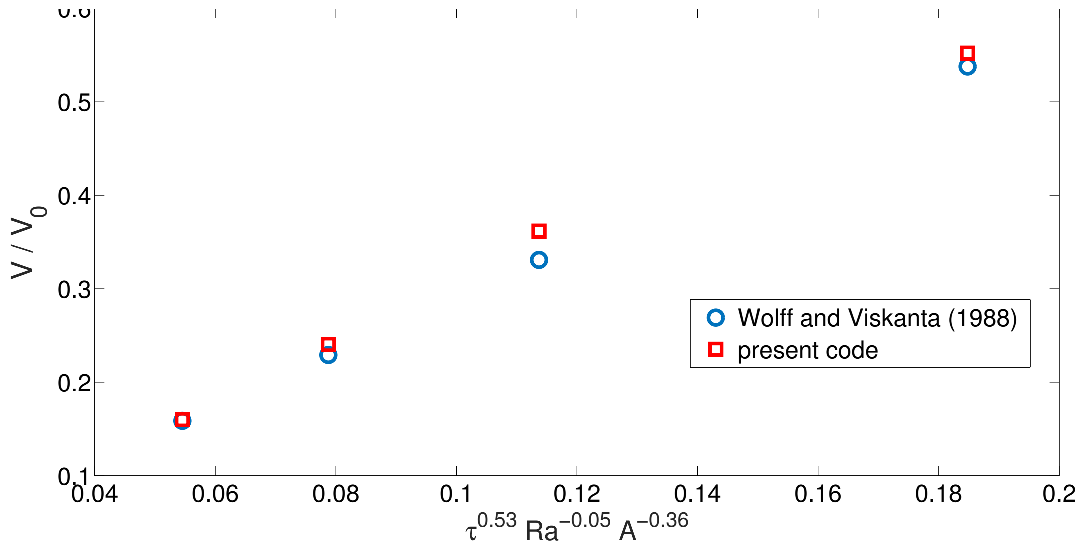

Figure 3: Comparisons of solidified volume fraction for data available in Ref. [41]

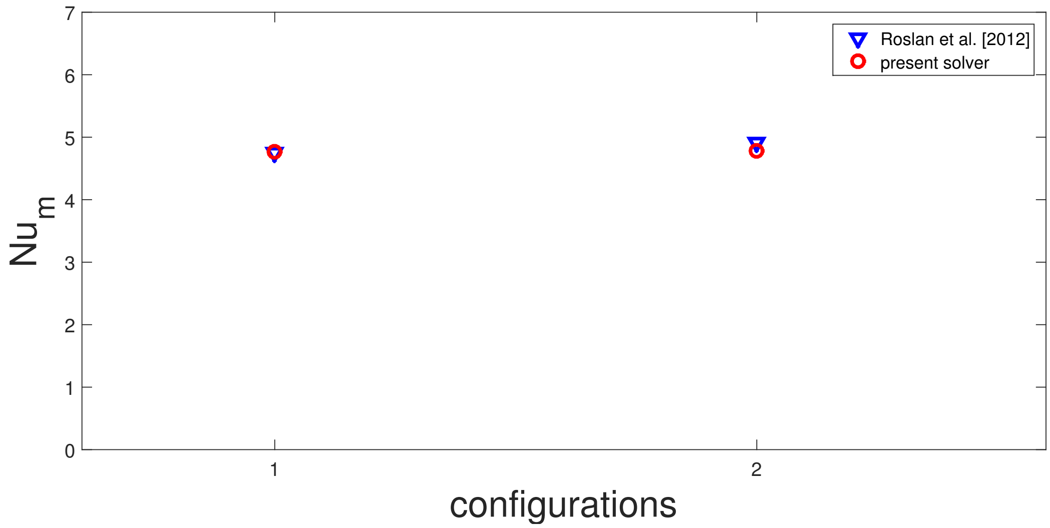

Figure 4: Average Nu comparison in a cavity with an inner rotating cylinder (configuration 1: R=0.1, $\Omega = 500$ and configuration 2: R=0.2, $\Omega = 1000$, Reference values in [42] were used.)

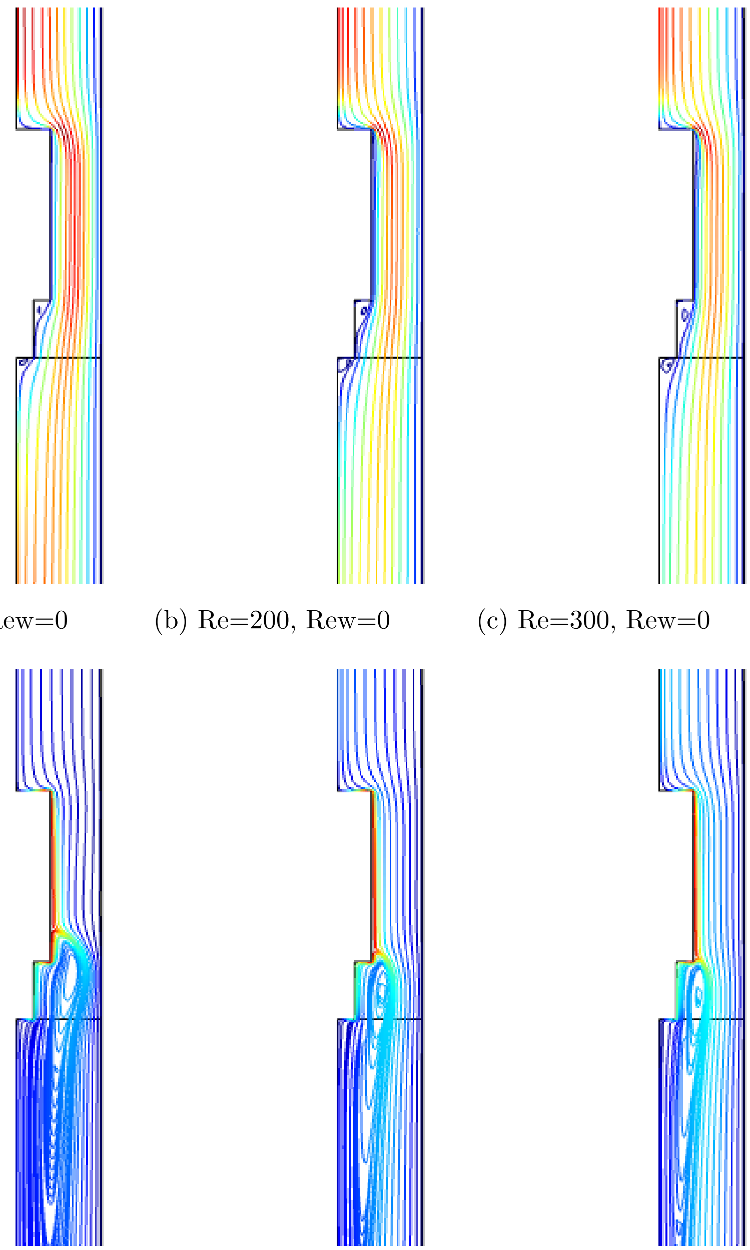

(a) Re=100, Rew=0 (b) Re=200, Rew=0 (c) Re=300, Rew=0

(d) Re=100, Rew=300 (e) Re=200, Rew=300 (f) Re=300, Rew=300

Figure 5: Influence of Re on the flow patterns at two different values of Rew ($L1d = 0.1L, L2d = 0.5L, H2d = 0.3H2$)

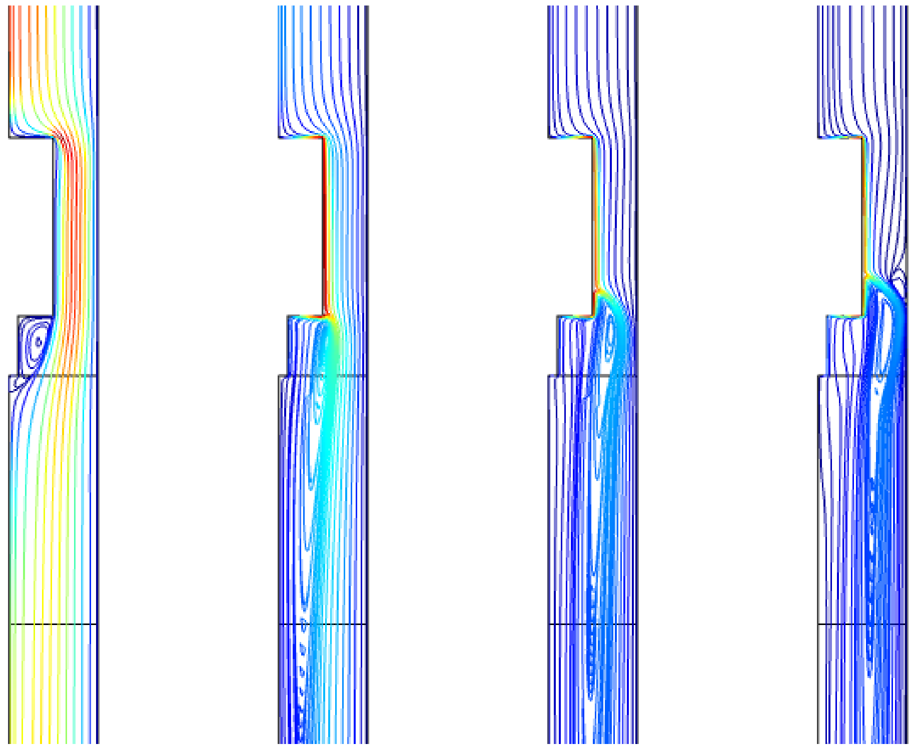

(a) Rew=0 (b) Rew=50 (c) Rew=150 (d) Rew=300

Figure 6: Effects of Rew on the flow patterns (Re $= 200, L1d = 0.1L, L2d = 0.5L, H2d = 0.3H2$)

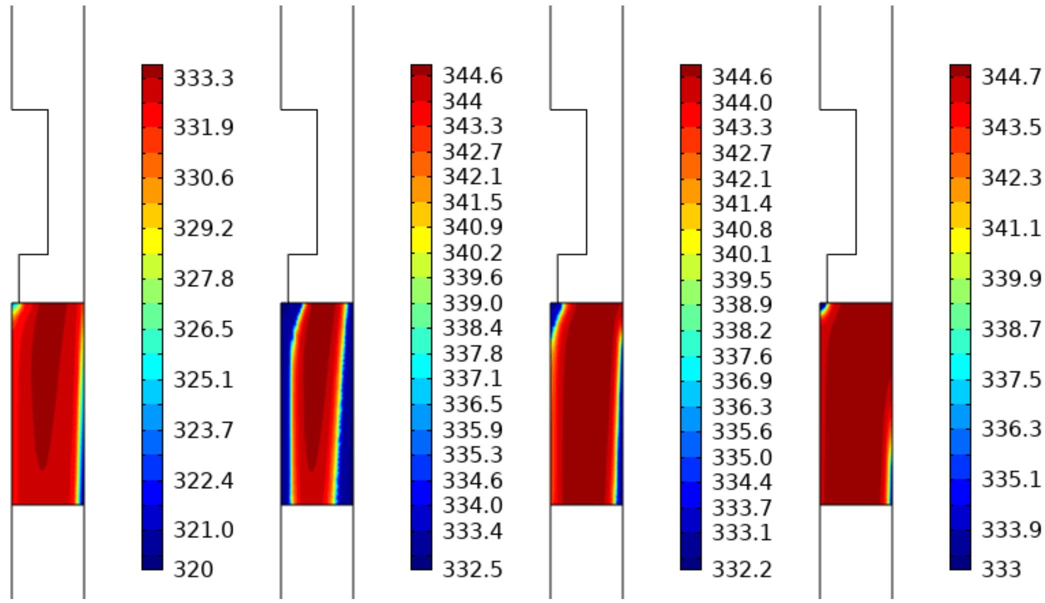

(a) Rew=0, t=10 (b) Rew=0, t=20 (c) Rew=0, t=30 (d) Rew=0, t=40

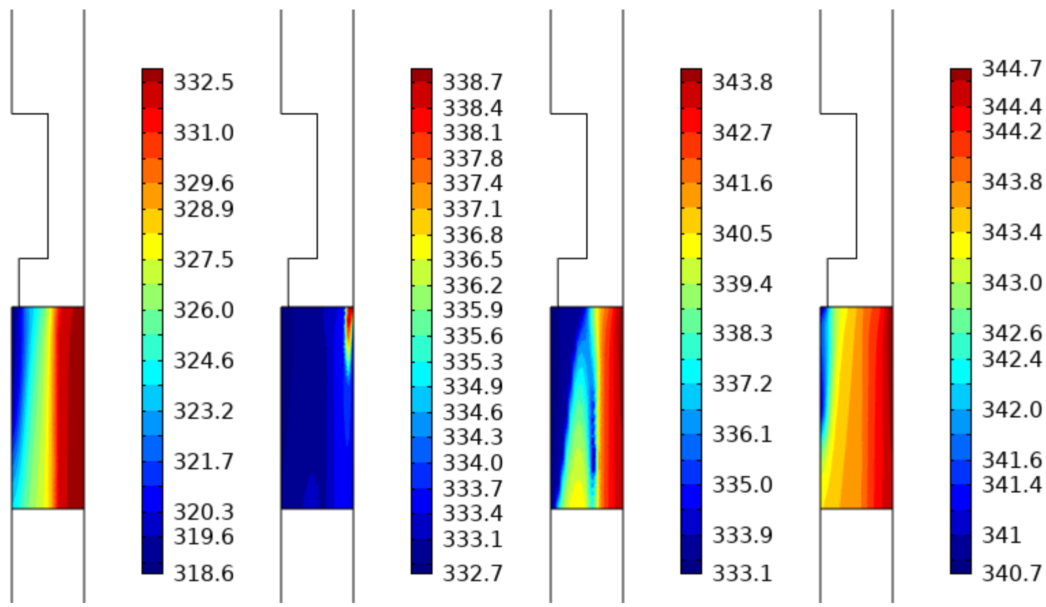

(e) Rew=300, t=10 (f) Rew=300, t=20 (g) Rew=300, t=30 (h) Rew=300, t=40

Figure 7: Effects of Rew on Tp at various time instants in minutes (Re $= 200, L1d = 0.1L, L2d = 0.5L, H2d = 0.3H2$)

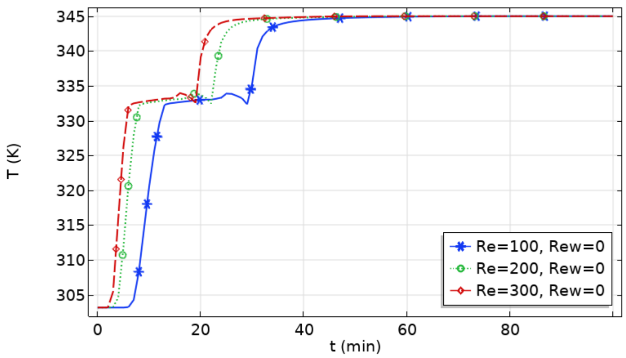

(a) Rew=0, mid point

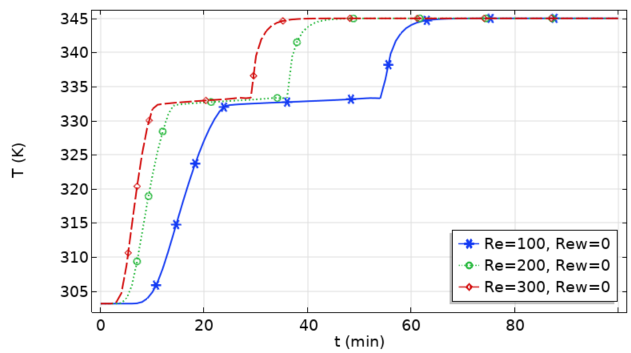

(b) Rew=300, wall point

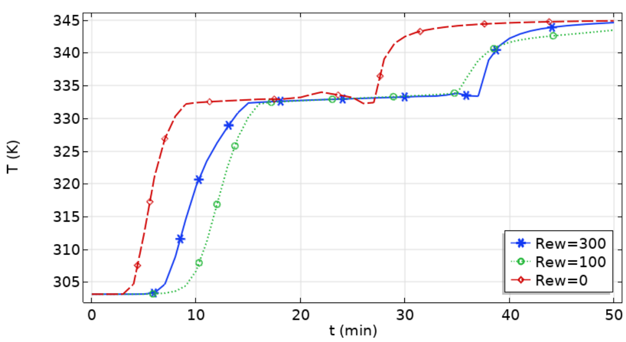

(c) Re=200, mid point

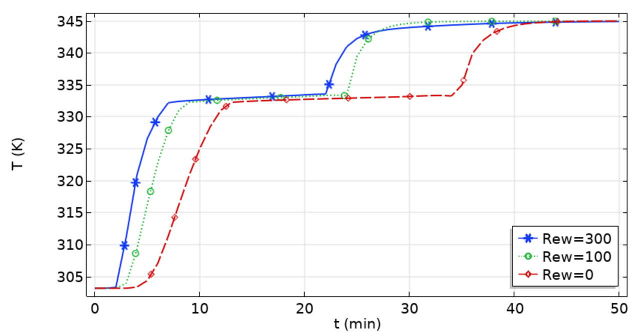

(d) Re=200, wall point

Figure 8: Influence of Re and Rew on the PCM temperature at two different points ($\mathrm{Re} = 200, L1d = 0.1L, L2d = 0.5L, H2d = 0.3H2$)

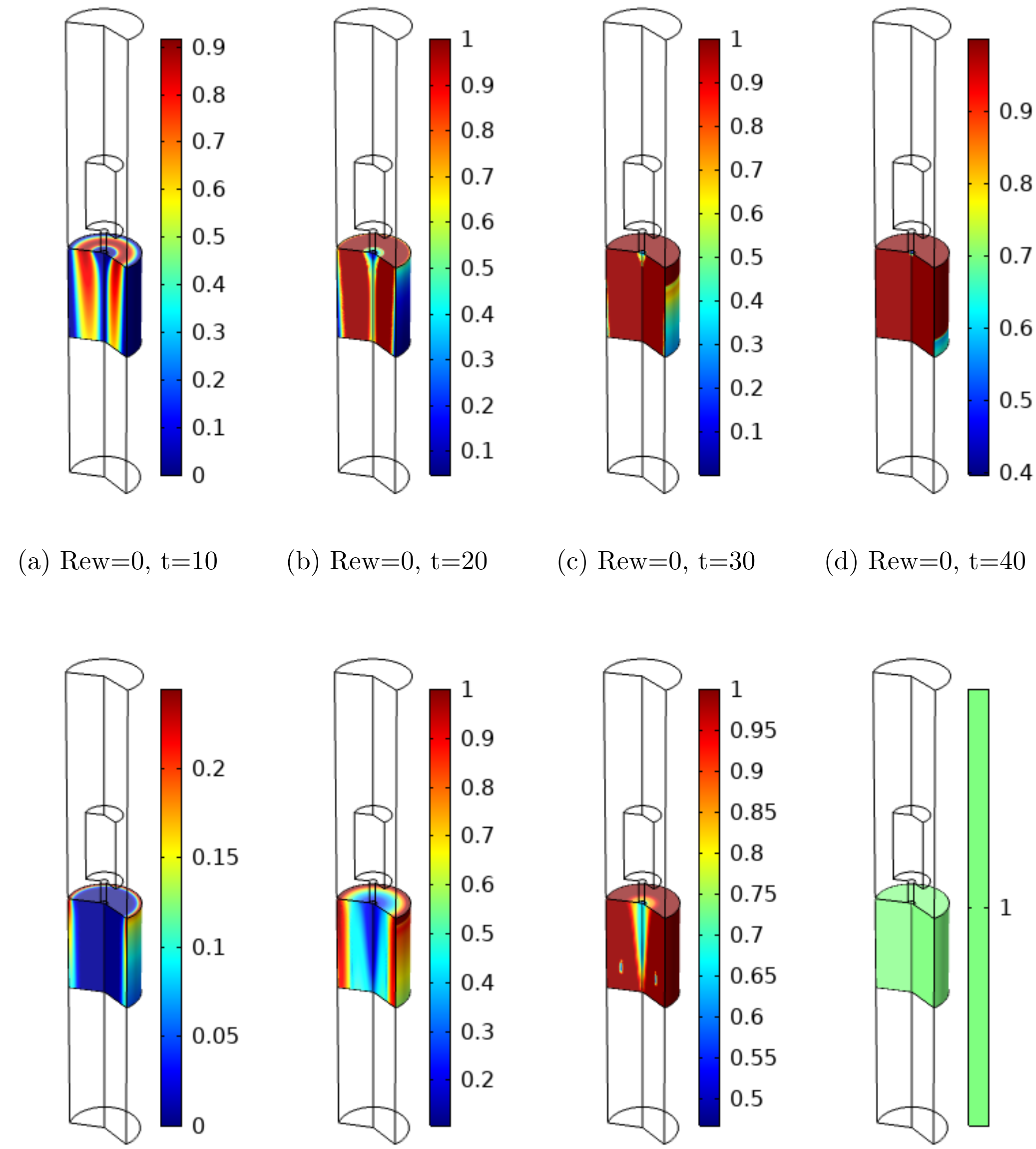

(a) Rew=0, t=10 (b) Rew=0, t=20 (c) Rew=0, t=30 (d) Rew=0, t=40

(e) Rew=300, t=10 (f) Rew=300, t=20 (g) Rew=300, t=30 (h) Rew=300, t=40

Figure 9: Effects of Rew on Lf at various time instants in minutes (Re $= 200, L1d = 0.1L, L2d = 0.5L, H2d = 0.3H2$)

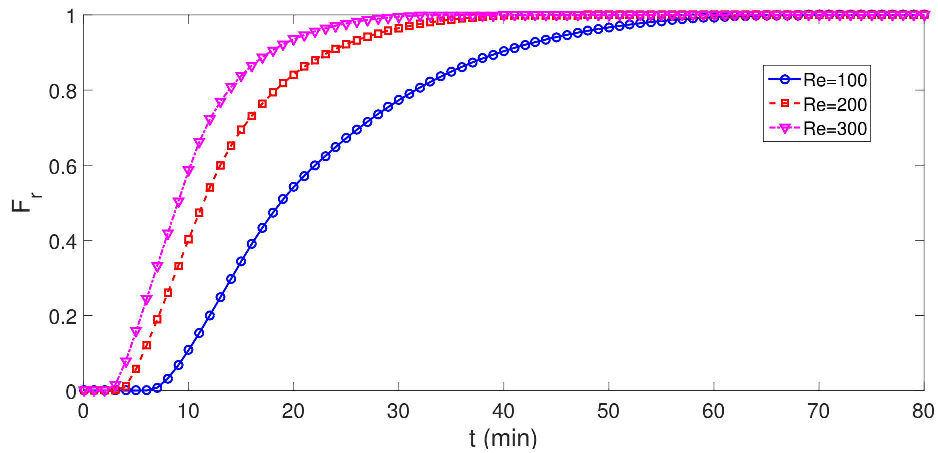

(a) Rew=0

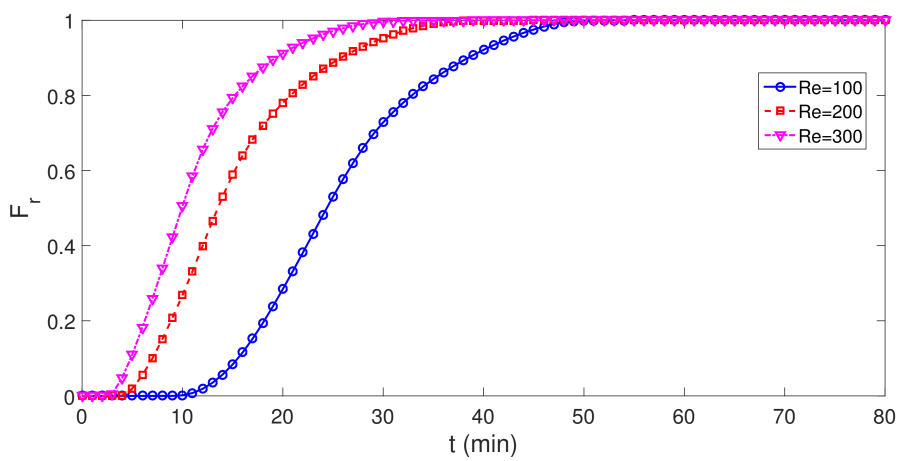

(b) Rew=300

Figure 10: Time evolution of F_r for different Re at two different values of Rew (Re = 200, $L1d = 0.1L, L2d = 0.5L, H2d = 0.3H2$)

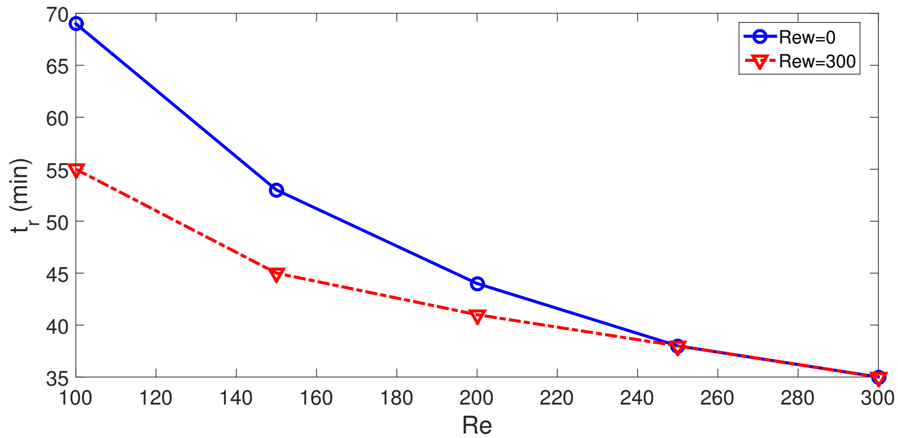

(a)

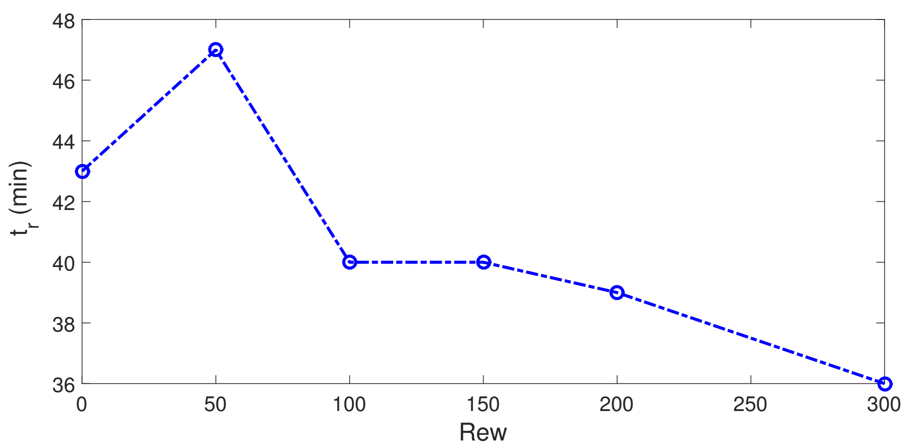

(b) Re=200

Figure 11: Effects of Re and Rew on the phase transition time ($L1d = 0.1L, L2d = 0.5L, H2d = 0.3H2$)

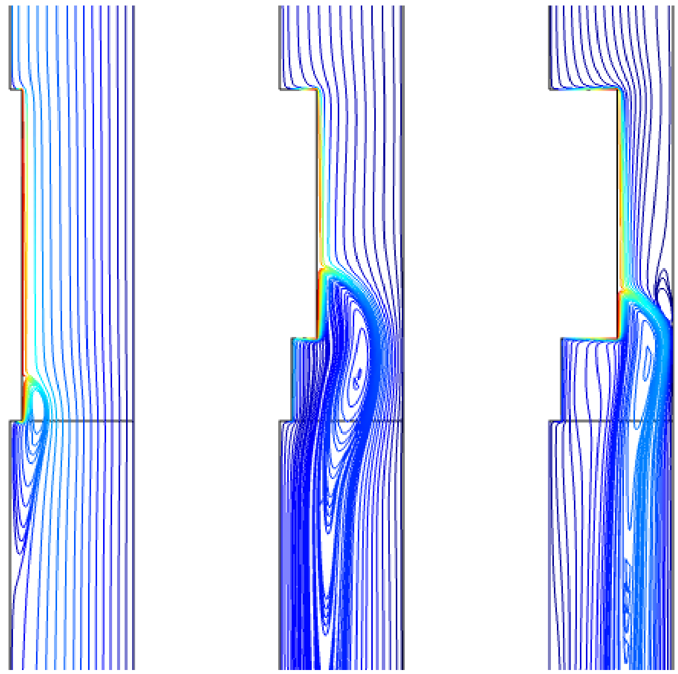

(a) L2d=0.1L (b) L2d=0.3L (c) L2d=0.55L

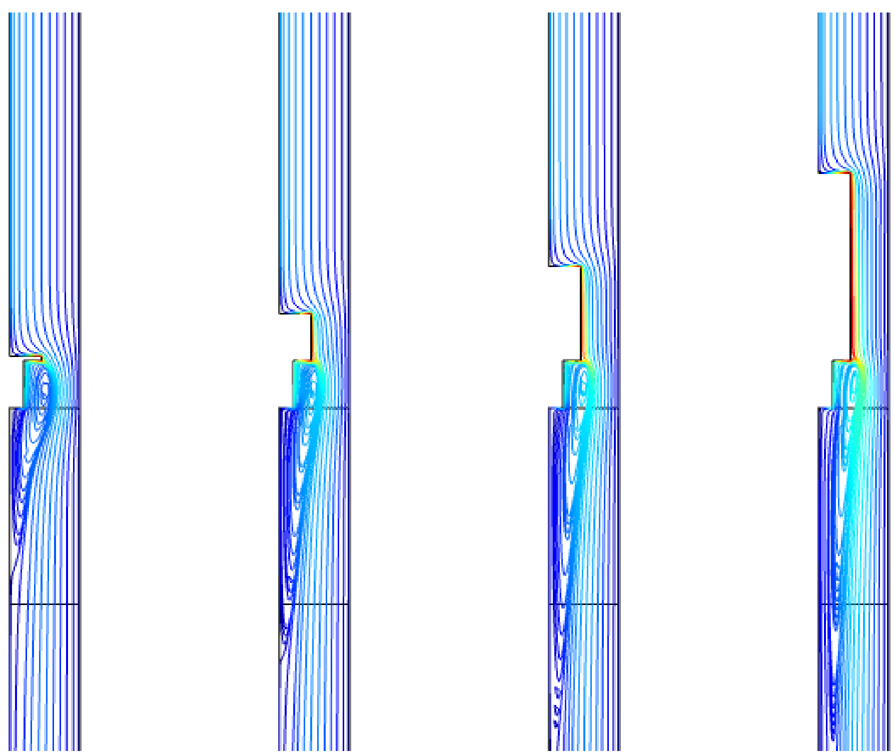

(d) H2d=0.001H2 (e) H2d=0.01H2 (f) H2d=0.02H2 (g) H2d=0.04H2

Figure 12: Effects of rotating disk length and height on the flow patterns (Re = 200, Rew=250, L1d=0.1L)

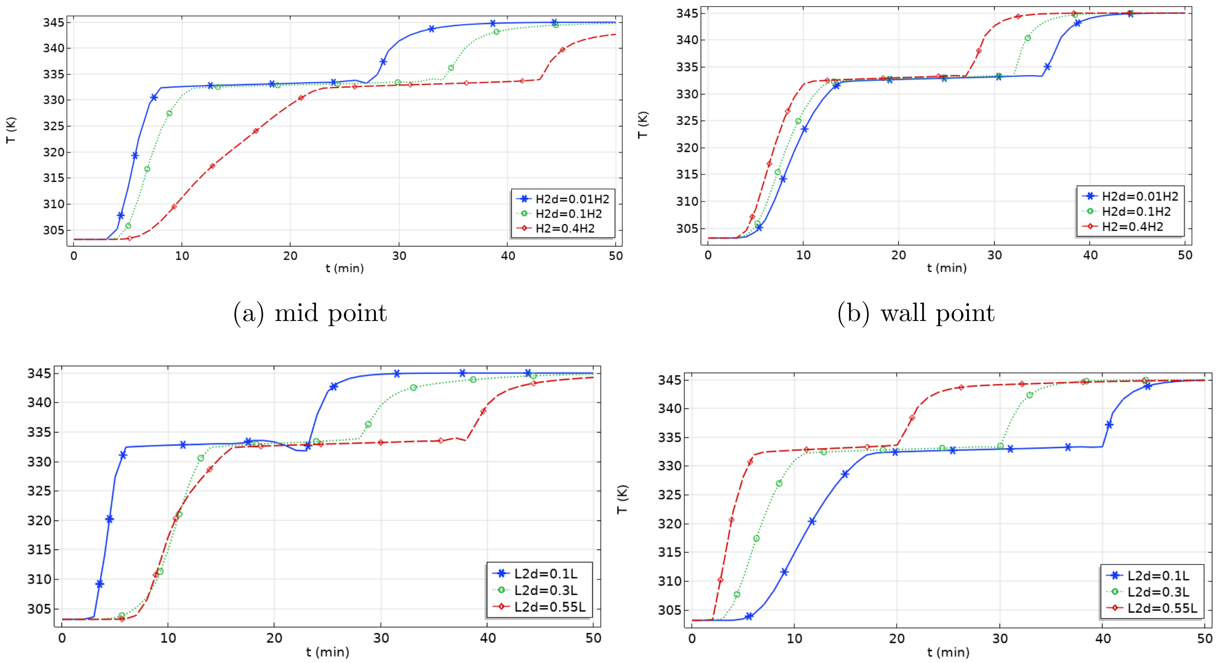

(a) mid point (b) wall point

(c) mid point (d) wall point

Figure 13: Effects of inner rotating disk height (a-b) and length (c-d) on the PCM temperature variations (Re = 200, Rew=250, L1d=0.1L)

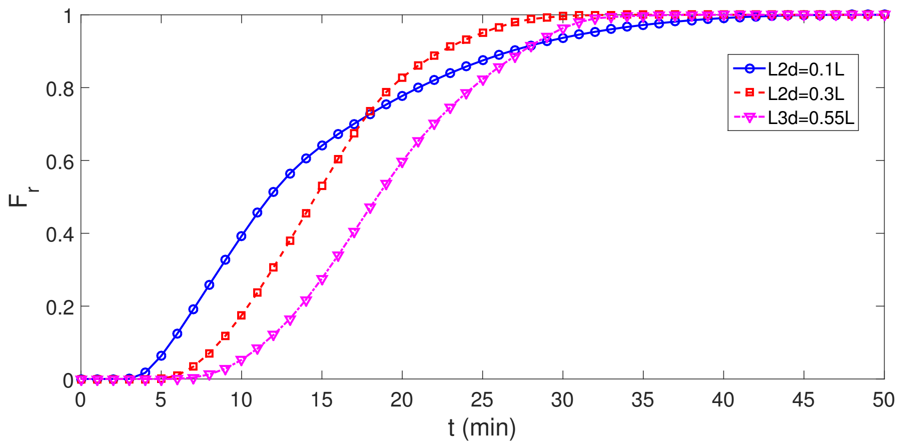

(a)

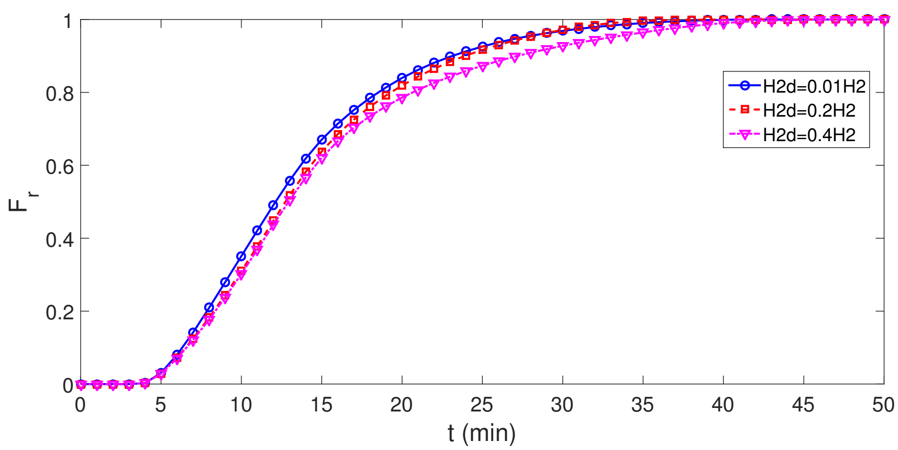

(b)

Figure 14: Time evolution of F_r for different length (a) and height (b) of the inner rotating disk (Re = 200, Rew=250, L1d=0.1L)

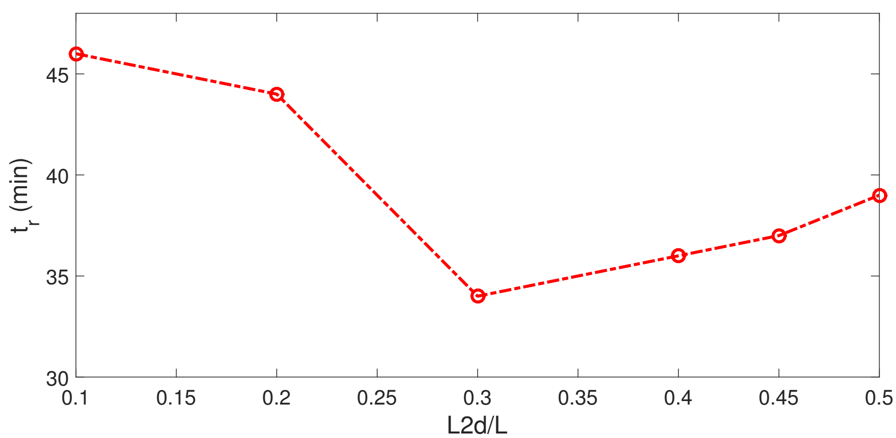

(a)

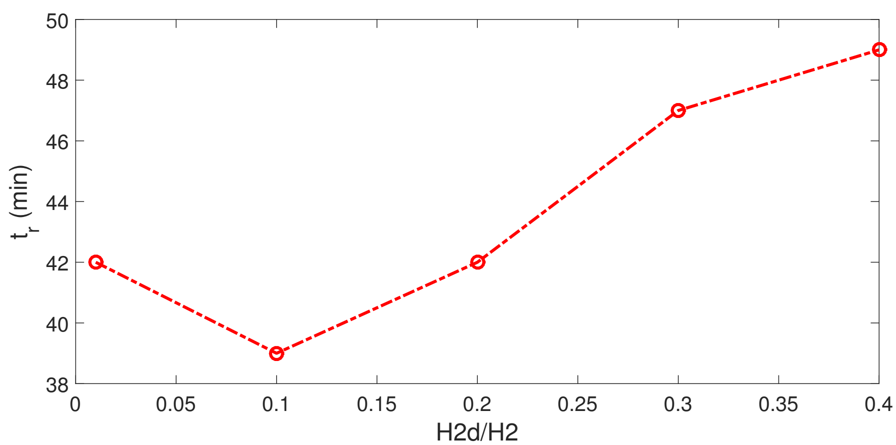

(b)

Figure 15: Impacts of full phase transition time for different length (a) and height (b) of the inner rotating disk (Re = 200, Rew=250, L1d=0.1L)

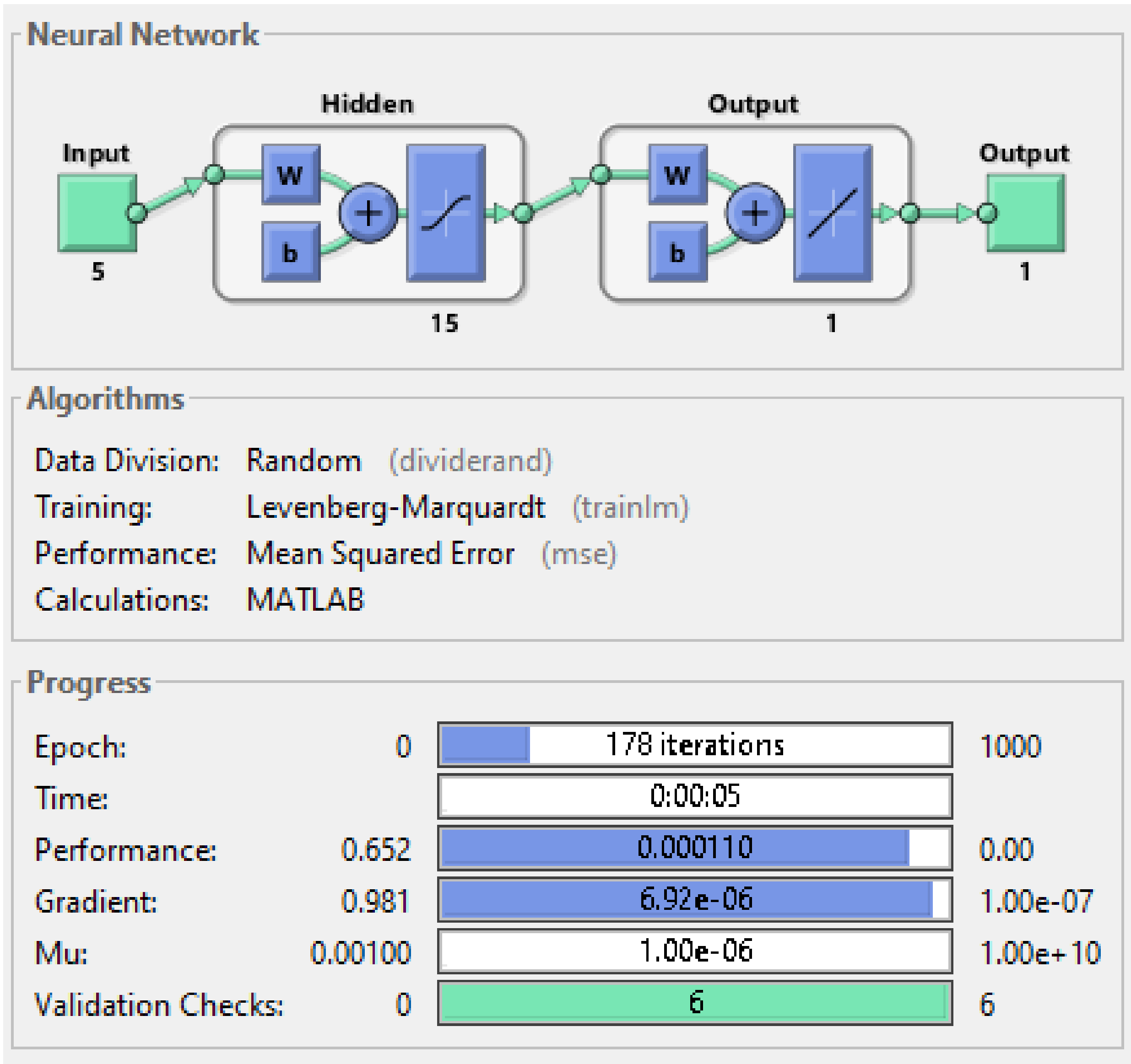

Figure 16: ANN model properties

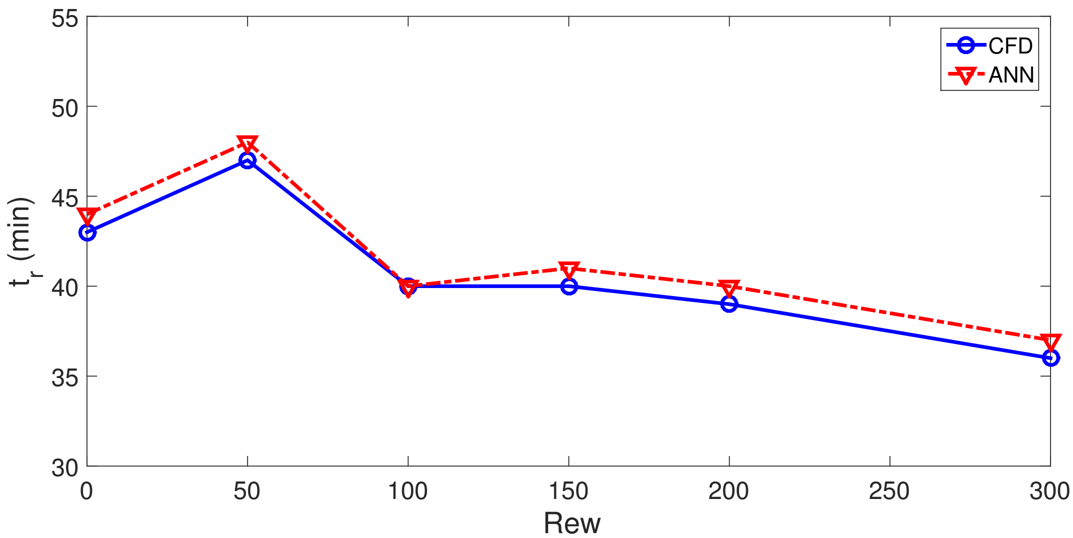

(a)

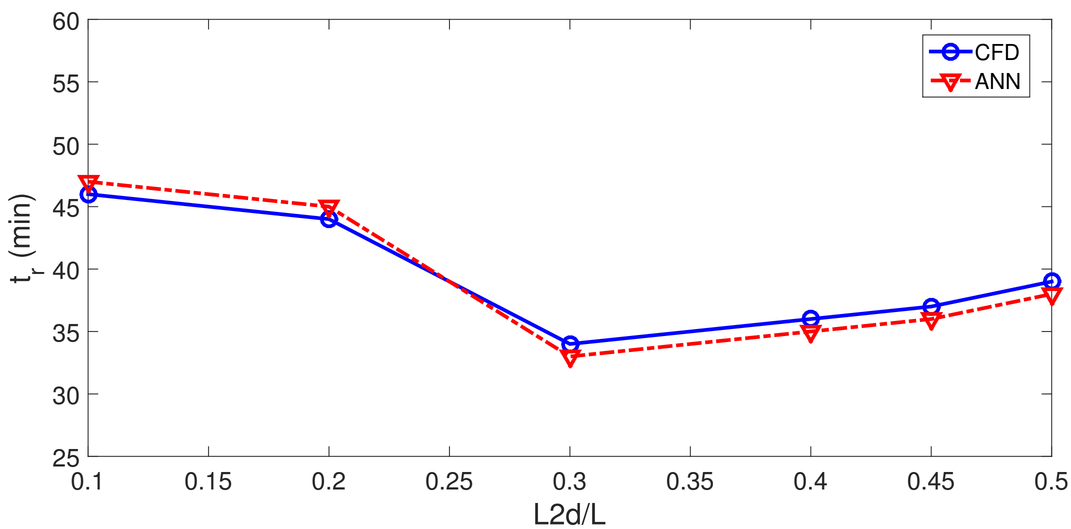

(b) Rew=300

Figure 17: Comparisons of ANN and CFD results in predicting the full phase transition time for varying Rew (b)